


Continuous-wave generation of photon pairs in silica nanofibers using single-longitudinal- and multilongitudinal-mode pumps

Philippe Delage¹, Tao Liu¹, Ewan Mer¹, Maha Bouhadida¹, and Sylvie Lebrun

Université Paris-Saclay, Institut d'Optique Graduate School, Centre National de la Recherche Scientifique, Laboratoire Charles Fabry, 91127 Palaiseau, France

 (Received 2 April 2021; revised 28 October 2021; accepted 29 November 2021; published 27 December 2021)

In this paper, we describe experimental observation and characterization of emission of photon pairs through four-wave mixing (FWM) in a silica nanofiber, with high coincidence to accidental ratio (CAR, at best greater than 20 000 in the cw regime at pump power 24 mW and 40 000 in the pulsed regime at pump power $\approx 150 \mu\text{W}$) and high pair emission rate (above 1 MHz in the pulsed regime with CAR around 100 at pump power $\approx 7 \text{ mW}$), despite residual presence of Raman spontaneous scattering (in the vicinity of the 12th silica Raman band) on the idler side. Moreover, these pairs of photons are observed with either a single-longitudinal-mode source or a multimode source (as well as a pulsed source) showing a factor of 2 increase of emission rate with the multimode source thanks to its random temporal fluctuation coupled to the quadratic response of FWM.

DOI: [10.1103/PhysRevA.104.063715](https://doi.org/10.1103/PhysRevA.104.063715)

I. INTRODUCTION

Sources of photon pairs are traditionally based on spontaneous parametric down-conversion which can be indifferently operated either in the cw or in the pulsed regime [1,2]. Synchronous and asynchronous quantum protocols were then developed in both regimes, such as the ones using energy-time entanglement in the cw regime and its equivalent in the pulsed regime, the time-bin entanglement [3,4]. With the development of spontaneous four-wave-mixing (FWM) integrated sources, both regimes continue to be explored depending on the used structures, pulsed operation in waveguides [5], and cw operation in resonant systems (ring cavities, coupled resonator optical waveguides, etc.) [6]. For fibered structures, the easier to operate pulsed regime remains the preferred regime used in applications and the cw regime fibered generation of pairs of photons has long been searched for but has given few results [7–11].

There are several reasons for that difficult search. The main one is related to the quadratic power response of the FWM mechanism used to generate these photon pairs that leads to much less efficiency and lower generation rates compared to the preferred pulsed regime. The second reason is the simultaneous presence of spontaneous Raman scattering, that generates a large quantity of noise photons that will mask the pairs. The broadband nature of the Raman emission spectra of silica, compared to crystalline materials such as silicon [5,6,12], to liquids [13], or even to materials such as noble gases that do not present Raman transitions [14,15], will prevent any frequency filtering of these photons. This will be thus a major limitation of the use of silica fibers as sources of pairs of photons. Due to its linear power dependence, spontaneous Raman scattering is even more of a problem in the cw regime that often prevents one from seeing the much smaller quadratic signature of the number of detected photons

in cw experiments [9] (even if the use of the coincidence detection reveals the pairs). In order to eliminate the deleterious influence of Raman scattering in silica fibers, low-temperature operation [8,9,11] can be used, with the drawbacks of a higher experimental complexity. Another possibility is the use of a large frequency shift of the photon pairs [7,10] but with incomplete elimination due to the residual presence of higher-order Raman bands [7].

Large frequency shifts are generally obtained by using either photonic crystal fibers [7,10,16], that thanks to their small core diameters present properly positioned zero dispersion wavelengths (ZDWs), or birefringent fibers [17] using vectorial four-wave mixing. One possible alternative is the use of tapered micro- and nanofibers [18–20]. The nanofibers are easily fabricated from a standard fiber by pulling it above a flame. Any value for the nanofiber waist size can be chosen in the micrometer and the submicrometer range [21], with length that can reach several centimeters (up to tens of centimeters [22]). The nanofiber is conceived and fabricated together with the tapers that connect it to the standard fibers, which means that extremely high transmission (typically greater than 90%) can be obtained and potentially lossless coupling of photons in and out of the nanofiber can be obtained. Pulsed generation of photon pairs in micro-nanofibers has already been demonstrated and is still the subject of intense research [23–27]; however, here we show the generation of photon pairs in the cw regime in these nanofibers.

Moreover, we demonstrate that the pair emission rate in the cw regime depends on the temporal modal contents of the pump, with a two times higher emission rate measured with a multimode pump. The experiment is based on two classical laser sources used in nonlinear optic experiments, first a tunable pulsed (picosecond) mode-locked Ti:sapphire laser, and a distributed Bragg reflector single-longitudinal-mode laser diode. Both sources emit in the near infrared and

are used around 852 nm (the laser diode wavelength). The Ti:sapphire laser (Tsunami from Spectra-Physics) is pumped by a cw green laser and is actively mode locked to deliver short pulses with pulse duration in the picosecond range [autocorrelation full width at half maximum (FWHM) duration around 2 to 6 ps] at a high repetition rate of 80 MHz. When mode locking is disabled, the emitted beam becomes cw (with the same average power), but the laser emits light in a highly multilongitudinal-mode regime (necessary to obtain short pulses by locking all the modes), and the beam presents high-speed random temporal fluctuations that average to the mean power. We will thus be able to directly compare our single-photon source operation in these three temporal regimes (mode-locked pulses, multilongitudinal-mode cw, and single-longitudinal-mode cw).

II. CHOICE OF THE NANOFIBER CHARACTERISTICS

This pump is sent in the nanofiber that will be our nonlinear medium. Photon signal (S) and idler (I) frequencies are created with a spectral probability of emission characterized by the joint spectral intensity (JSI) [28] that is written as the product of two functions related to energy ($2\omega_P - \omega_S - \omega_I = 0$) and momentum ($2\beta_P - \beta_S - \beta_I = 0$) conservation (Appendix A). The size and length of the nanofiber are chosen to have best performances with the chosen pump wavelength (around 852 nm) in order to generate an idler photon in the telecom band (around 1550 nm), and thus a signal photon through energy conservation in the visible range (around 580–590 nm). The simulation (Appendix B) shows that for our experimental conditions the nanofiber radius has to be in the 412-nm range [23]. The length of the nanofiber should be as long as possible to reach a high emission efficiency, but with the constraint that the nanofiber radius should stay uniform within several tenths of 1% on that range. In our case, a nanofiber length of 1 cm appeared to us a good compromise considering the performance of our pulling platform to realize a good generation rate (at the expense of a slightly higher pump power to compensate for the reduced length) and a near ideal phase matching sinc shape.

The nanofiber is connected to the initial SMF28 fiber by tapers that are realized simultaneously with the nanofiber during the “pull and brush” fabrication procedure. The procedure’s ability to effectively realize the designed nanofiber and tapers has been previously validated, using a home-made shape measurement optical system [21] and scanning electron microscope measurements [29]. We designed the tapers with parameters giving symmetric adiabatic tapers (21-mm length each) that allow us to realize a virtually lossless coupling of light from the fundamental mode of the SMF28 fiber core to the nanofiber (for more details about conditions to be fulfilled in order to obtain adiabatic tapers, see, for example, Ref. [30]). The nonlinear object thus consists in connectorized SMF28 access fiber (typical length 40 cm), the entrance taper followed by the nanofiber (radius 412 nm, length 1 cm), and the output taper and a second connectorized SMF28 access fiber (typical length 40 cm) (see inset in Fig. 1). The ensemble (tapers and nanofiber, with a global length of 5.2 cm) is fixed in a glass box to manipulate it easily and to protect it, as best as possible, from ambient dust.

Once a nanofiber is pulled and prepared with fiber connectors, we first realize a transmission measurement test, to verify the nanofiber integrity and have a first idea of its quality and of our ability to inject the pump preferentially in the fundamental HE₁₁ mode of the nanofiber (even if the nanofiber and the SMF28 are slightly multimode, with a V parameter at pump wavelength around 4 in both cases, careful injection of light allows us to excite only the fundamental mode, with negligible coupling to high-order modes during propagation thanks to the adiabatic tapers). The typical raw transmission of a nanofiber (corrected from optical element losses) on our experimental setup is around 50–60%. It is, to standard experimental alignment fluctuations, identical to the one obtained with an unpulled SMF28 fiber prepared identically. This transmission is essentially limited by the Fresnel reflection losses of fiber connectors, by the quality of fiber cleaving, by the residual aberration present on the laser pump beam, and by the alignment quality. Freshly realized nanofibers have thus virtually no propagation and tapers coupling losses. Nevertheless, after some time (i.e., at least several months), we observe some decrease of the nanofiber raw transmission, probably due to accumulation of dust in the vicinity of the nanofiber waist (correlated to apparition of punctual scattering points on the nanofiber waist, not initially present on the freshly pulled fiber). After almost one year the raw transmission of the nanofiber used in this study decreases around 30%, attributed to propagation losses in the nanofiber waist part with a transmission of the nanofiber going from ≈ 1 to ≈ 0.6 , indicating that the protecting glass box was not totally hermetic [31].

III. EXPERIMENTAL SETUP

The nanofiber is inserted in the experimental setup shown in Fig. 1. The pump beams are coupled to the access entrance fiber together with probe beams at 633 nm (He-Ne laser) and at telecom wavelengths (1520–1620-nm tunable laser diode) using a dichroic mirror. These additional lasers are used for alignment optimization of the detection channels. The tunable laser diode is additionally used to characterize the photon pair emission spectrum (joint spectral intensity) through a stimulated emission tomography (SET) experiment [32–34]. The pump beam power is varied before the injection using a $\lambda/2$ -polarizer setup. At the output of the nanofiber (i.e., at the output of access SMF28 fiber) the beam is collimated and sent to dichroic mirrors first to extract the high-power pump beam, and then to separate the signal and idler photons. Additional high- and low-pass filters as well as interferential band-pass filters are used to further eliminate residual scattered pump photons. Signal photons are coupled to a SM780 fiber, whereas idler photons are coupled to a SMF28 fiber and coupled to additional fibered filters (coarse wavelength division multiplexing (CWDM) filters or tunable filter). Then the fibers are connected to single-photon detectors, a Geiger mode silicon avalanche photodiode (APD) for the signal photon detection (Aurea technology module), and a Geiger mode InGaAs APD (ID230 module from IDQuantique) for idler photon detection. Both APDs deliver TTL pulses corresponding to the detected photons and are connected to a computer-controlled counter and tem-

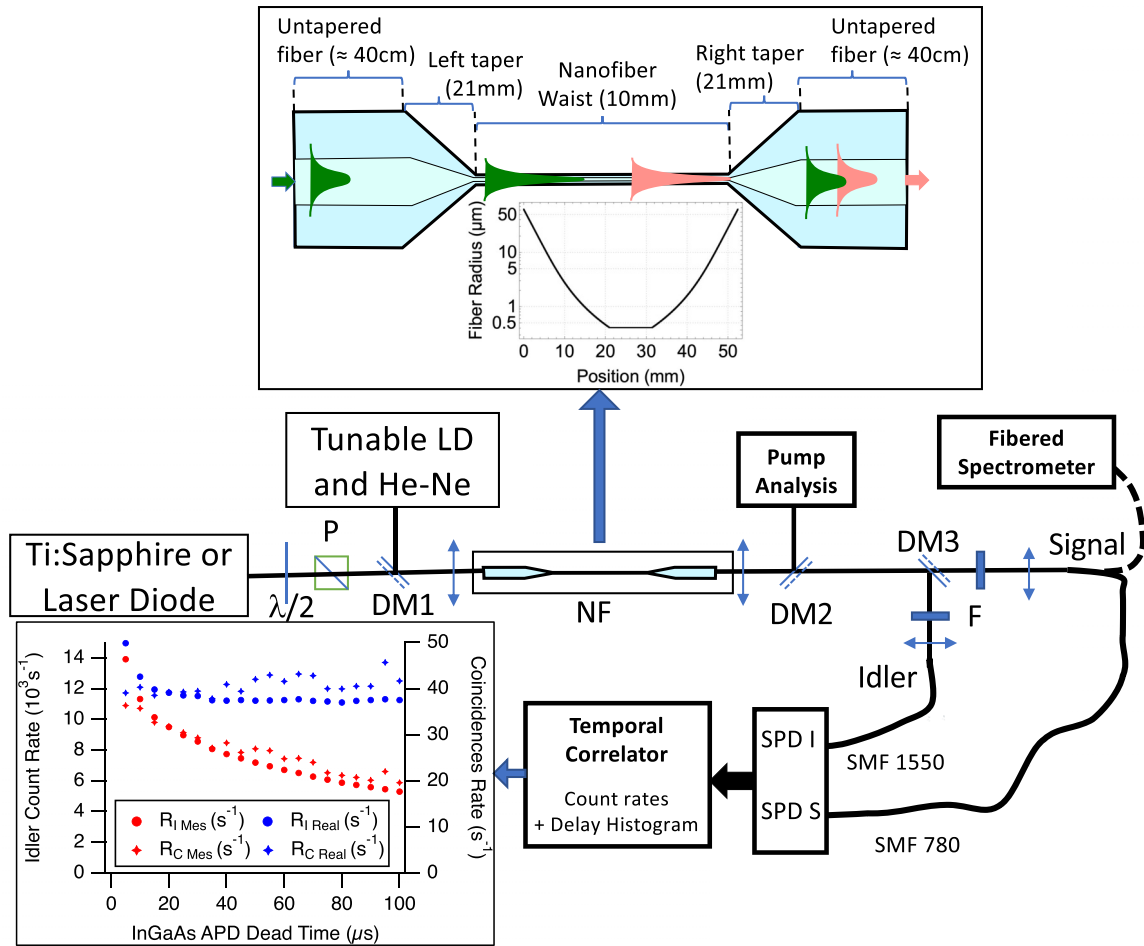


FIG. 1. Schematic of the experimental setup (DM, dichroic mirrors; P, polarizer; $\lambda/2$, half-wave plate; F, high-pass, low-pass, or band-pass spectral filters). Light collected from the nanofibers is injected in single-mode fibers (SMF), connected to different characterization instruments, and to single-photon detectors (SPD) for idler and signal wavelengths, followed by a temporal correlator for counts measurement and coincidence analysis (additional fibered components, CWDM or tunable filters, or couplers, not shown here, might also be used). The upper inset shows the global nanofiber structure, with a plot of the designed shape of the adiabatic tapers realized by the pulling platform. The lower inset shows a plot of real (blue/dark gray symbols) and measured (red/gray symbols) detector count and coincidences rates showing the effect of deadtime correction on the acquired data.

poral correlator device (ID900 module from ID Quantique). Fibers can also be connected to power meters or optical spectrum analyzers and a fibered spectrometer, for setup characterization and SET measurements. An extracted pump beam is also sent to a multimode fiber for pump spectrum measurement or to a power meter for transmitted power measurement.

We thus measure the signal and idler photon count rates, $R_{S \text{ meas}}$ and $R_{I \text{ meas}}$ (s^{-1}), respectively, received by the two detectors, as well as coincidence histograms between the signals of the two detectors from which we deduce the coincidence rate $R_{C \text{ meas}}$ (s^{-1}) from the number of samples detected in the coincidence peak (in a temporal window $t_{\text{bin}} = 1.3 \text{ ns}$ corresponding to the width of the coincidence peak) and normalized to the measurement duration (typically between 10 s and 1 h depending on measurement power and temporal regime). These measured data are corrected for the deadtime of the detectors ($\tau_{\text{DT } I} = 20 \mu\text{s}$

and $\tau_{\text{DT } S} = 33 \text{ ns}$) to give the actual count and coincidence rates

$$R_{S,I \text{ real}} = \frac{R_{S,I \text{ meas}}}{(1 - \tau_{\text{DT } S,I} R_{S,I \text{ meas}})}, \quad (1)$$

$$R_{C \text{ real}} = \frac{R_{C \text{ meas}}}{(1 - \tau_{\text{DT } S} R_{S \text{ meas}})(1 - \tau_{\text{DT } I} R_{I \text{ meas}})}, \quad (2)$$

that will be the ones analyzed ultimately. We have verified these expressions (see lower inset in Fig. 1), at least for the InGaAs detector, the deadtime of which can be adjusted and for which deadtime correction is more critical. The real values calculated for these experimental conditions are then deadtime independent (in contrast to the measured value) except for the detector count rate at low deadtime where the influence of the detector after-pulses becomes dominant (all the presented data in the paper used $\tau_{\text{DT } I} = 20 \mu\text{s}$ chosen as a compromise to prevent detector saturation at high counting rates and a

moderate after-pulse probability value around 10% [35] that allows us to neglect their influence in first approximation).

IV. PHOTON PAIR EMISSION IN CW AND PULSED REGIMES

The nanofiber is first characterized using an SET [32] experiment (Appendix C), for an easy and rapid measurement of the JSI that characterizes the emission spectra of the source. This allows a precise alignment of the experiment. The measured JSI is the same whatever the pump temporal regime and is very close to the expected sinc shape, with nevertheless small side lobes attributed to fluctuation of the nanofiber diameter [36]. That shape is compatible with the one caused by a sinusoidal fluctuation (Appendix D) of the ZDW with a period of 3.83 mm and an amplitude of 2.2 nm (around the reference value of $\lambda_{\text{ZDW}} = 1036$ nm). Such a variation of the ZDW corresponds to a variation of the diameter of the nanofiber of about ± 2 nm, around the mean diameter of 824 nm, showing a very good uniformity of the nanofiber.

Then, the signal and idler photon count rates, R_S and R_I , as well as coincidence histograms between the signals of the two detectors from which we deduce the coincidence rate R_C (s^{-1}) are measured as a function of the mean power of the pump beam for the different temporal regimes. The results are shown in Fig. 2.

A. Analysis of photon pairs measurement

First, we see in Fig. 2 a clear quadratic response (line of slope 2 on the used log-log scale) for the different quantities except for the idler detector in the cw regimes (red/gray triangle and disks), that presents a linear response. Moreover, that idler count rate is almost identical for both cw pump sources (either single or multimode). This indicates that despite the very-high-frequency shift (almost 700 nm between idler and pump) the idler counts are still dominated by the Raman response of the silica nanofibers, even if for that frequency shift the idler is in the vicinity of the 12th silica Raman band (i.e., much farther than in previous measurements [7,23]). In the pulsed regime, as expected, the FWM quadratic contribution is much higher and clearly dominates. In contrast, on the signal side (blue/dark gray triangle and disks) the quadratic dependence indicates a complete absence of Raman scattering contribution (which is, with such shifts, naturally orders of magnitude smaller on the anti-Stokes side than on the Stokes side) and the quadratic response is observed even in the cw regime at very low power (after correction from the detector dark count contribution). Here, the quadratic response of the detector count rate is seen in the cw regime for fibered structure; the Raman contribution of the anti-Stokes side prevented reaching quadratic behavior previously [9].

In the pulsed regime the clear quadratic evolution of counts and coincidence shows that we can consider we are in an almost Raman-free FWM contribution similar to the one studied in Ref. [15]. By comparing coincidence rate ($R_C = \eta_S \eta_I \mu_P \bar{I}^2$, with \bar{I} the mean pump power and μ_P the pair generation efficiency coefficient at the nanofiber exit) to signal and idler count rates ($R_{S,I} = \eta_{S,I} \mu_P \bar{I}^2$) in this pulsed regime, we deduce the signal ($\eta_S = 12\%$) and idler ($\eta_I = 5\%$) detection

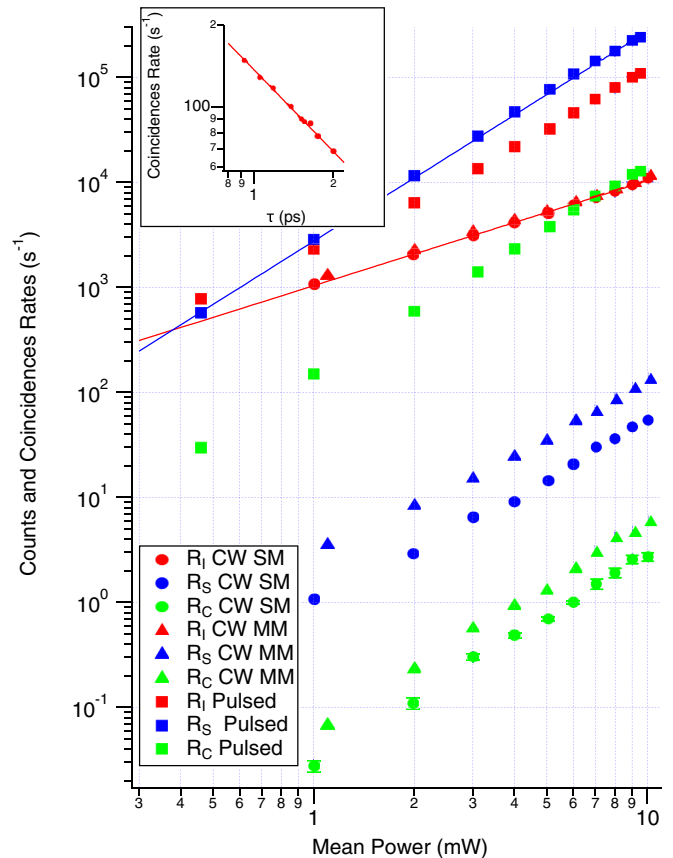


FIG. 2. Intensity dependence of the idler count rate (red/gray symbols), signal count rate (blue/dark gray symbols), and coincidences rate (green/light gray symbol), for the pulsed pump source (square symbols), the longitudinally multimode cw pump source (CW MM, triangle symbols), and the longitudinally single-mode cw pump source (CW SM, disk symbols). The lines show the main quadratic (blue/dark gray line) and linear (red/gray line) power dependences. The mean power is measured at the nanofiber output, after the dichroic mirror used to extract the pump beam. The presented idler and signal count rates are subtracted from the independently measured dark count rate of the used detectors ($\text{DCR}_I = 65 \text{ s}^{-1}$ and $\text{DCR}_S = 53 \text{ s}^{-1}$). The errors bars on the measurement are about the size of the symbols and are only shown for the coincidences rate of the single-mode cw pump. The autocorrelation FWHM of the pulse for this experiment was 2.8 ps [corresponding to a pulse duration $\tau = 1.03$ ps for the hyperbolic secant pulse $I(t) = I_0 \text{sech}^2(\frac{t}{\tau})$]. The inset shows the variation of the coincidences rate as a function of the pulse duration with an adjustment with a function $A\tau^{-1}$.

efficiencies of our measurement setup (often identified to the heralding efficiency). These detection efficiencies include the quantum efficiency of the detectors ($\text{QE}_S = 56\%$ and $\text{QE}_I = 21\%$) and the transmission losses of the detection channels (that consisted in the optical losses of the different optical elements for about half of the losses, and the injection losses of the detected beams in the collection single-mode fibers of our fibered single-photon detectors, injection losses that are typically lower than 50% depending on alignment optimization). All the measurements of Fig. 2 having been realized on the same day without requiring any readjustment of the detection stage (only the pump injection in the nanofiber had

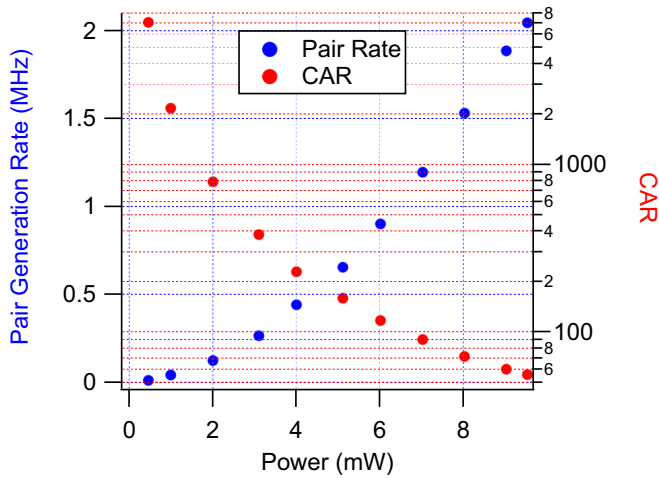


FIG. 3. Plot of the pair generation rate (i.e., coincidences rate corrected from detection efficiencies), and CAR in the pulsed regime pumped at 852 nm. The generation rate reaches 2 MHz with a CAR value of 56, at a moderate pump power of 9.5 mW. This generation rate is similar to the one obtained in the literature [24]; with at least a three times higher CAR, the higher power used here (9.5 mW, instead of 2 mW) allows us to compensate for the smaller length of the nanofiber and the slightly longer pulse duration.

been possibly reoptimized when switching between different temporal regimes) these values are then supposed to be identical in the cw regime (the previous simple treatment is not possible in this regime due to the Raman contribution).

To go beyond this first rapid and qualitative analysis of the response in the different regimes, we adjust all the experimental data presented in Fig. 2 with a second-order polynomial function. We here concentrate on the most significant results for our quantitative analysis (the complete analysis and results of these adjustments are presented in Appendix E). The linear coefficient term of the idler count rate will be related to the Raman contribution; we found values of $1031 \pm 14 \text{ s}^{-1} \text{ mW}^{-1}$ with the cw single-mode source, $1088 \pm 14 \text{ s}^{-1} \text{ mW}^{-1}$ with the cw multimode source, and $1183 \pm 41 \text{ s}^{-1} \text{ mW}^{-1}$ in the pulsed regime. These coefficients in the three regimes are found to be very close, as expected for an effect that is directly related to the mean power of the pump beam. The second important parameter is the quadratic coefficient term of the coincidence rate related to the four-wave-mixing nonlinear efficiency. We found values of $0.0291 \pm 0.0028 \text{ s}^{-1} \text{ mW}^{-2}$ with the cw single-mode source, $0.0570 \pm 0.0044 \text{ s}^{-1} \text{ mW}^{-2}$ (i.e., 1.96 times higher) with the cw multimode source, and $146.5 \pm 3.4 \text{ s}^{-1} \text{ mW}^{-2}$ (i.e., 5034 times higher) in the pulsed regime. As expected, the pair generation efficiency is higher in the pulsed regime, but we also measure a two times higher efficiency with the multimode source compared to the single-mode source. Considering the detection efficiencies, the generated pair rate at the output of the nanofiber reaches $\mu_P = 24 \times 10^3 \text{ pairs s}^{-1} \text{ mW}^{-2}$ in the pulsed regime, i.e., at 10-mW power a pair generation rate of 2 MHz (Fig. 3) that corresponds to less than 2.5×10^{-2} pairs per pulse, a value sufficiently low to consider the generation of multiple pairs as negligible. This rate is similar to the one already observed in nanofibers [24] with just a slightly higher operating power

allowing us to compensate for the smaller nanofiber length and the longer pulse duration. In the cw regime we have, as expected for a nonlinear mechanism with quadratic response, a lower generation rate $\mu_P = 5 - 10 \text{ pairs s}^{-1} \text{ mW}^{-2}$ which corresponds to a generation rate of the order of 12 kHz at a power of 35 mW, a value which is only 25 times smaller than the one of a commercial spontaneous parametric down conversion source [37] (with a possibility to close the gap using a higher pump power in the range of 200 mW that can be accessible relatively easily with the usual sources, especially if we consider that multimode pumps are beneficial in our case).

B. Source intensity-distribution influence on pair generation

The change of nonlinear performance with the modal content of cw sources has already been observed and analyzed in the context of classical nonlinear optics [38,39]. It is observed here in the context of a quantum source of a pair of photons based on a nonlinear phenomenon. This change of behavior is due to the fact that the temporal statistics of the highly multimode source is close to the one of a thermal source [40,41] and that the nonlinear response will be affected by that statistics. The multimode source presents temporal spikes that may have high peak powers and that will generate nonlinearly more pairs in a short period of time. To quantify this effect and estimate the efficiency in the different regimes, we use the model of Ref. [40] in which it is shown that the nonlinear efficiency of a nonlinear mechanism which depends on the n th power of a pump beam intensity is related to the n th-order moment $\langle I^n \rangle = \int_{-\infty}^{\infty} I^n P(I) dI$ of the intensity distribution $P(I)$ describing the pump beam statistics [and verifying $\int_{-\infty}^{\infty} P(I) dI = 1$]. For the single-mode cw pump, we have evidently $P(I) = \delta(I - \bar{I})$, and for the multimode source we use the usual expression $P(I) = \frac{1}{\bar{I}} e^{-I/\bar{I}}$ of a thermal source [38–40]. Finally, for the pulsed source we rederived the expression $P(I) = -\frac{2}{T} \frac{1}{dI/dt}$ developed for a Gaussian pulsed source [40] to the case of our pulsed source that delivers hyperbolic secant pulses $I(t) = I_0 \text{sech}^2(\frac{t}{\tau})$ (with duration τ , pulse period T , and peak intensity $I_0 = \frac{\bar{I}T}{2\tau}$) [42], to obtain $P(I) = \frac{\tau}{T} \frac{1}{I\sqrt{1 - \frac{I}{I_0}}}$.

Considering the nonlinear mechanisms observed in our experiment, the spontaneous four-wave-mixing efficiency (defined as the number of pairs generated per second) will be given by the second-order moment $\langle I^2 \rangle$, whereas the spontaneous Raman scattering will be related to the first-order moment $\langle I \rangle$ (in contrast to the case of the stimulated regime of Raman amplification treated in Ref. [39]). The calculations of these moments for the different regimes are summarized in Table I. The main result is the confirmation of the expected observation of a two times better photon pair emission in the case of the multimode cw source for the spontaneous four-wave-mixing mechanism. We can note that this improvement is not expected in the case for the spontaneous parametric down conversion for the emission of photon pairs [43], or for the third-order spontaneous parametric down conversion for the emission of photon triplets [44], as these mechanisms, similarly to the spontaneous Raman scattering, are governed by the first-order moment.

TABLE I. Parameters for the evaluation of relative nonlinear efficiencies for a given mean intensity \bar{I} , for the single- and multimode cw sources and the pulsed sources delivering hyperbolic secant pulses (with a duration $\tau = 1.03$ ps and a pulse period $T = 12.5$ ns).

Source characteristics	Intensity distribution $P(I)$	First-order moment $\langle I \rangle$	Second-order moment $\langle I^2 \rangle$	Raman relative intensity	Theoretical pair generation relative efficiency	Experimental pair generation relative efficiency
cw single-mode	$\delta(I - \bar{I})$	\bar{I}	\bar{I}^2	1	1	1
cw multimode	$\frac{1}{T} e^{-I/T}$	\bar{I}	$2\bar{I}^2$	1	2	1.96
Sech pulsed	$\frac{\tau}{T} \frac{1}{1 + \sqrt{1 - I/I_0}}$	\bar{I}	$\frac{2}{3} \frac{I_0^2}{\tau} = \frac{T}{3\tau} \bar{I}^2$	1	4050	5034

When compared to experimental generation efficiencies one obtains a good accordance between the predictions of the model and the experiments; especially, the better performance of the highly multimode cw Ti:sapphire laser is correctly explained. Identically, the order of magnitude of the difference between the pulsed and the cw regime is also correctly evaluated. The slightly better than expected efficiency in the pulsed regime might be due to a better injection of the pump beam for that particular experiment illustrated by a slightly better transmission of the nanofiber (32% instead of 28% in the cw regime at the time of the experiment).

The expression in the pulsed regime shows that the efficiency is governed by the peak-average power product or, said a different way, that it is inversely proportional to the pulse duration. This last variation is only valid if all the photons are collected by the detection setup, that can be a problem with very short pulses as the JSI is broadened inversely proportionally to the pulse duration [34]. In our experimental condition, this relation is still valid and was confirmed experimentally (see inset in Fig. 2) on the short range of variation of the pulse duration allowed by the laser dispersion control system (τ varying from 1 to 2 ps).

V. CAR MEASUREMENTS

A. CAR in the different temporal regimes of the pump

To characterize the performances of the nanofiber as a source of a pair of photons we need to characterize the CAR. The coincidences were measured previously by counting the number of counts in the coincidence peak. The accidentals are measured by counting the counts outside this coincidence peak. The exact measure depends on the temporal regime. In the pulsed regime, we clearly see (see inset in Fig. 4), in the coincidence histogram, peaks with a temporal separation equal to the repetition period T of the laser. The noise excess in these periodic peaks is mainly due to occurrence between unpaired parametric photons of different pulses [15] (i.e., a photon of a pair the twin photon of which has not been detected in the other branch). We thus measure the mean number of counts in a large number of peaks (typically 300 on each side of the coincidence peak) in a temporal window equal to the one used to measure the number of counts in the coincidence peak (i.e., $t_{\text{bin}} = 1.3$ ns). In the cw regime, the measure is simpler as all time bins outside the coincidence peak contribute in the same manner to the noise. We then just measure the average number of counts in a large temporal window on both side of the coincidence peak, here again nor-

malized in the same temporal window as the coincidence peak measurement. These measurement protocols allow us to extract the measured parameter from a large number of samples, i.e., with a low error bar (calculated supposing a Poissonian noise statistics), with moderate measurement duration (typically some tens of minutes and most of the time less than 1 h) even in the case of very high CAR and low powers. For the experimental conditions of Fig. 2, we measured a maximum value of the CAR of 7000 in the pulsed regime (Fig. 3), 2300 in the single-mode cw regime, and 2700 in the multimode cw regime. These values are of the order of magnitude of the best values observed in fibered structures [10, 15, 17], despite being still limited first by the Raman contribution on the idler side

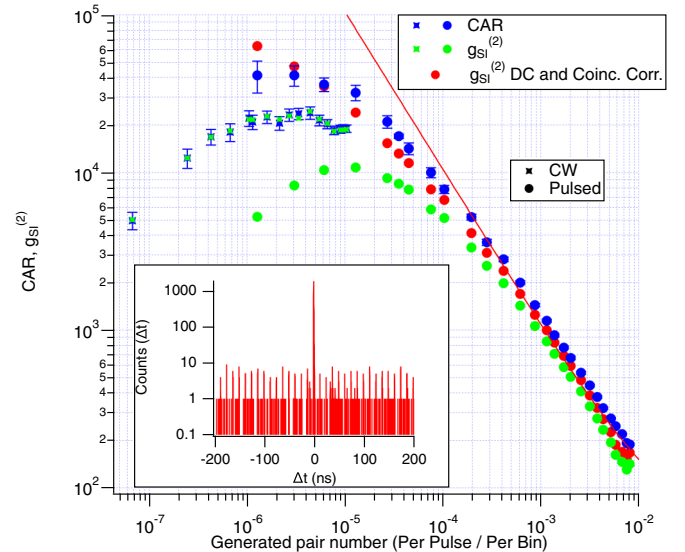


FIG. 4. Measured CAR (blue/dark gray symbols) and calculated $g_{SI}^{(2)}$ (green/light gray symbols) as a function of the generated number of pairs per pulse (p) in the pulsed regime ($\tau = 1.4$ ps) (disks) and per bin in the multimode cw regime (diamonds). The red/gray line is a guideline indicating a p^{-1} variation. The red/gray symbols represent the calculated $g_{SI}^{(2)}$ corrected from the dark count contribution and from the coincidence contribution to the signal and idler count rates (see text for precisions). The pump wavelength was 839 nm in both experiments; we estimated $\eta_S = 9\%$ and $\eta_I = 5\%$ in the pulsed regime and $\eta_S = 8\%$ and $\eta_I = 1\%$ in the cw regime, the lower idler detection efficiency being due to the higher loss induced by the use of the tunable filter compared to the CWDM filter used in the pulsed experiment. The inset shows a typical coincidence histogram in the pulsed regime at a mean power of 5.13 mW with a CAR of 450 (acquisition time 10 s).

and second to a lower extent by the dark counts on the signal side.

B. Optimization of the CAR

To decrease Raman scattering and increase the CAR, we first choose to shift Ti:sapphire pump wavelength to 839 nm. The idler beam being shifted to 1550 nm, the wavelength shift between pump and idler photons is thus increased by 30 nm. This allows us to go from a situation where we are in the vicinity of the 12th Raman peak of silica (at 440 cm^{-1}) to a situation where we pass this peak and are on the beginning of the leading edge of the much lower 13th Raman peak. The second improvement used for cw experiment (in the pulsed regime the source can still be considered as virtually Raman free) was to use a smaller width band-pass filter by replacing the CWDM filter by a tunable filter that reduces the almost white Raman noise. We choose a filter with a width of 3 nm centered on the central peak of the JSI. We lose some of the parametric pairs, due to this filtering (only 40% of the emitted spectra passes the filter, that would normally be able to detect the whole JSI peak if the fiber had been perfectly uniform) and because of the lower (around 40%) transmission of the filter, but nevertheless obtain a better signal to noise ratio. These different improvements allow us to reduce the Raman count by more than two orders of magnitude (Appendix E), without nevertheless completely eliminating it (the idler counts still varying linearly with the pump power). We also benefit from the two times higher emission rate of pairs due to the multimode nature of the pump (no single-mode laser diode was available at that wavelength for comparison). The signal and idler counts and coincidences rates have a similar behavior as in the previous measurement and results of polynomial adjustment of the power dependences are shown in Appendix E.

We first characterize the CAR in the cw regime, measured as a function of the generated pair numbers per bins (given by $p = \frac{R_C}{\eta_S \eta_I} t_{\text{bin}}$ in the cw regime) still for a value $t_{\text{bin}} = 1.3 \text{ ns}$ corresponding to the width of the coincidence peak. Considering that most of the detected counts on the detectors are in fact contributing to noise, the CAR can be identified (see blue/dark gray and green/light gray diamond in Fig. 4) to the normalized second-order correlation defined as $g_{SI}^{(2)} = \frac{R_C}{R_S R_I t_{\text{bin}}}$ in the cw regime [10]. This allows for an evaluation of the CAR by considering only the detector counts and coincidences rates.

CAR (and $g_{SI}^{(2)}$) reaches a value of $24\,000 \pm 2000$ at a pump power around 24 mW and a generation rate around 5 kilocounts/s (see Appendix F for an alternate analysis of $g_{SI}^{(2)}$ and comparison with the present state of the art).

We then characterize the CAR in the pulsed regime; the experimental setup is almost identical to the one for Fig. 2 except that we use the 1550-nm output of the CWDM filter (as the Raman noise is not as critical as in the cw regime), and a slightly longer pulse duration $\tau = 1.40 \text{ ps}$ compared to the pump at 852 nm. The results are presented in Fig. 4 (blue/dark gray disks) as a function of the generated pair number per pulse (given here by $p = \frac{R_C}{\eta_S \eta_I} T$). As expected from the CAR model [15] CAR varies as p^{-1} for high p , until a saturation at low p due to the influence of dark counts. CAR is always higher than 100 even at the highest generation rate around 1 megacount/s at 8-mW power and reaches values as high as $41\,000 \pm 6000$ for an average pump power $\approx 100 - 150 \mu\text{W}$.

If we calculate the normalized second-order correlation ($g_{SI}^{(2)} = \frac{R_C}{R_S R_I T}$) adapted to the pulsed regime [17], we see that this parameter (green/light gray disks in Fig. 4) clearly underestimates the CAR, both in the high pair number regime and in the low pair regime, even if in both cases the reason is different. In the high pair number regime, R_S and R_I that are used to estimate the accidental include a non-negligible amount of coincidence counts (all the more so if the detection efficiency is high) that in practice do not participate in the accidental (as they are already counted as real pairs). These R_C have thus to be subtracted from the count rates R_S and R_I [or equivalently $g_{SI}^{(2)}$ has to be divided by $(1 - \eta_S)(1 - \eta_I)$ [15]]. For low number of generated pairs, the underestimation is due to the influence of the dark counts that are implicitly supposed to fully contribute to the accidental. This problem is usually solved by correcting R_S and R_I from the dark count rates [17] but in that case $g_{SI}^{(2)}$ is shown to vary as p^{-1} [15] without saturation at low power (see the line in Fig. 4) and thus with a clear overestimation of the CAR. In fact, in the pulsed regime the dark count photons are dispatched on all time bins when the accidentals are calculated only for some time bins synchronous to the pulse. In contrast to Ref. [17], we thus choose to correct only partially for the dark count by taking into account the ratio of the accidental time measurement window t_{bin} to the repetition period T . The corrected expression that takes into account both these effects is

$$g_{SI}^{(2)} = \frac{R_C}{\left[R_S - \left(1 - \frac{t_{\text{bin}}}{T} \right) \text{DCR}_S - R_C \right] \left[R_I - \left(1 - \frac{t_{\text{bin}}}{T} \right) \text{DCR}_I - R_C \right] T} \quad (3)$$

with $\text{DCR}_I = 65$ and $\text{DCR}_S = 53 \text{ s}^{-1}$ the dark count rate of the used detectors. It is shown as the red/gray disks in Fig. 4 and shows a good accordance with experimentally measured CAR. The small residual difference between $g_{SI}^{(2)}$ and CAR (red/gray and blue/dark gray circles in Fig. 4) is most probably due to the impact of detector after-pulses (estimated to $P_{\text{AP}} \approx 10\%$ for the InGaAs detector at the used deadtime value [35] and $P_{\text{AP}} \approx 0.5\%$ for the silicon detector) that causes an excess number of counts that will participate in the accidental (a

complete analysis of their exact influence on the CAR has still to be realized).

VI. CONCLUSION

We have thus observed generation of a pair of photons in the cw regime in a nanofiber structure. We have observed that temporal fluctuations due to the multimode nature of the cw pump beam induce a two times excess of pair generation

compared to a single-mode source, that has been analyzed in the context of nonlinear quantum sources of photon pairs. This result is also important for practical aspects as multimode sources are common in the field of nonlinear optics. For example, the largely used pulsed Ti:sapphire laser can easily be operated in the cw regime by stopping mode locking, which allows us to perform a rapid and direct comparison of the cw and the pulsed regime that nevertheless needs to consider the multimode nature of its cw operation for a correct comparison. The use of a multimode source is also interesting for future development from an application point of view as these sources are usually more powerful, easier to use, and cheaper than single-mode lasers.

The nanofiber geometry is very interesting as the nanofiber can be pulled with large length and controlled diameter that allows us to control phase-matching properties and emission efficiency. The nanofiber is pulled together with adiabatic tapers that allow us to assure almost lossless injection from the access fiber mode to the nanofiber mode. The obtained results are very promising considering the relatively small length (1 cm) of the nanofiber, and we have shown that such a nanofiber can be pulled with a relatively good uniformity, with diameter fluctuations of about ± 2 nm, sufficient to observe a close to ideal phase-matching curve shape. Controlling the nanofiber diameter on longer length will be the next objective of our study and results on the reproducibility of the nanofiber characteristics [30] make us feel confident in reaching that objective.

Finally, the realized source presents very good performances with pair emission rates that exceed 1 megacount/s in the pulsed regime and more than 1 kilocount/s in the cw regime for moderate pump power in the 10-mW range. Even if the performances are still limited by spontaneous Raman scattering (operated in the vicinity of the 12th Raman order), the source also presents CAR values largely above several thousands, with optimized maximum values of 41 000 and 24 000 in the pulsed and cw multimode regimes, respectively. These CAR values measured in the cw and pulsed regimes are, to the best of our knowledge, among the highest measured in a fiber structure geometry. This makes us confident in the possibility to observe even higher CAR in architectures where Raman scattering is reduced such as in fibers operated at low temperature [8] and used with improved superconducting detectors [10].

ACKNOWLEDGMENTS

This work is supported by the French National Research Agency (Grant No. FUNFILM-ANR-16-CE24-0010-03). Laboratoire Charles Fabry (LCF) is a member of Domaine d'Intérêt Majeur (DIM) Science et Ingénierie en Région Île-de-France pour les Technologies Quantiques (SIRTEQ) funded by Région Île-de-France.

APPENDIX A: JOINT SPECTRAL INTENSITY

The biphoton state created by a pump at frequency ω_P at the output of the nonlinear media is usually written, in the low efficiency regime, as [28,34,45]

$$|\psi(t)\rangle = |0, 0\rangle + \iint \mathcal{A}(\omega_P, \omega_S, \omega_I) |1_{\omega_S}, 1_{\omega_I}\rangle d\omega_S d\omega_I, \quad (\text{A1})$$

where the Joint Spectral Amplitude $\mathcal{A}(\omega_P, \omega_S, \omega_I)$ characterizes the emission spectra of the emitted pairs, and its square modulus the JSI [$\mathcal{I}(\omega_P, \omega_S, \omega_I) = |\mathcal{A}(\omega_P, \omega_S, \omega_I)|^2$], represents the probability of emission of a pair in a given spectral domain.

This Joint Spectral Amplitude (or Joint Spectral Intensity), except for a slowly frequency-dependent term related to the nonlinear efficiency of the medium (C , that will determine the efficiency of pair generation and will depend on multiple parameters including pulse energy and duration), is given by a product of two normalized functions related to energy and momentum conservation (see Fig. 5):

$$\mathcal{A}(\omega_P, \omega_S, \omega_I) = C g(\omega_P, \omega_S, \omega_I) \times f(\omega_P, \omega_S, \omega_I). \quad (\text{A2})$$

The energy conservation term depends on nonlinearity order and for spontaneous four-wave mixing it is given by $g(\omega_P, \omega_S, \omega_I) = [\tilde{G} * \tilde{G}](\omega_S + \omega_I - 2\omega_P)$, with $\tilde{G}(\omega) = T_F[G(t)]$ the Fourier transform of the normalized temporal shape $G(t)$ of the incident pulse amplitude. For the hyperbolic-secant pulse considered here, $G(t) = \text{sech}(t/\tau)$, an analytical expression for the normalized pulse autocorrelation spectra can be found: $[\tilde{G} * \tilde{G}](\omega) = (\pi\tau\omega/2)/\sinh(\pi\tau\omega/2)$. The width of this function [Fig. 5(a)] depends on the pulse duration becoming thinner when pulse duration increases (moving toward a Dirac function for a perfectly monochromatic pump). In the multimode cw regime, the multiple incoherent modes again broaden this function but

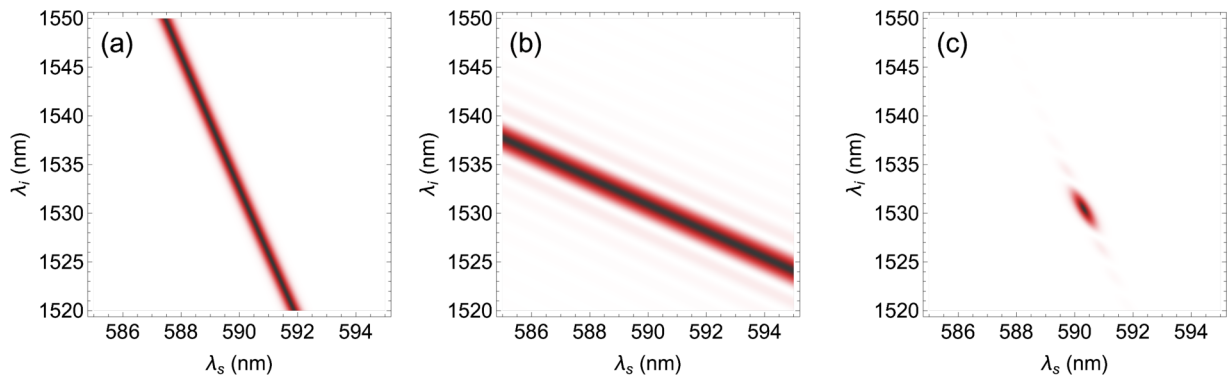


FIG. 5. Example of a plot of $|g(\omega_P, \omega_S, \omega_I)|^2$ (a), of $|f(\omega_P, \omega_S, \omega_I)|^2$ (b), and of their product (c) giving $\mathcal{I}(\omega_P, \omega_S, \omega_I) = |\mathcal{A}(\omega_P, \omega_S, \omega_I)|^2$ for a given pump wavelength. The calculation uses the typical parameters of the experiment.

without benefiting from the increasing of pulse peak power and then from the better efficiency brought by the phase locking of the mode in the pulsed regime.

The momentum conservation term $f(\omega_P, \omega_S, \omega_I) = \frac{1}{L} \int_0^L e^{-i \Delta\beta(\omega_P, \omega_S, \omega_I) z} dz$ depends on the phase mismatch of the nonlinear mechanism $\Delta\beta(\omega_P, \omega_S, \omega_I)$ and simplifies in a uniform nonlinear medium of length L , to the well-known phase-matching expression $f(\omega_P, \omega_S, \omega_I) = e^{-i \Delta\beta \frac{L}{2}} \text{sinc}(\frac{\Delta\beta L}{2})$.

APPENDIX B: NANOFIBER PROPAGATION PROPERTIES SIMULATIONS

The nanofiber is a kind of textbook object [46], which is perfectly theoretically described by a step index fiber model with a core of radius ρ and index n_{silica} surrounded by an infinite layer of air with index n_{air} . The effective index n_{eff} of the fundamental mode of the nanofiber, i.e., the HE_{11} vectorial mode considered here, is given by the eigenvalue equation (the equation and the described calculation can be easily generalized to any other propagation mode) [46]

$$\left(n_{\text{eff}} \frac{V^2}{U^2 W^2} \right)^2 = \left(n_{\text{silica}}^2 \frac{J_1(U)}{U J_0(U)} + n_{\text{air}}^2 \frac{K_1(W)}{W K_0(W)} \right) \times \left(\frac{J_1(U)}{U J_0(U)} + \frac{K_1(W)}{W K_0(W)} \right), \quad (\text{B1})$$

with $V^2 = U^2 + W^2$, $U^2 = \rho^2 \left(\frac{2\pi}{\lambda} \right)^2 (n_{\text{silica}}^2 - n_{\text{eff}}^2)$, and $W^2 = \rho^2 \left(\frac{2\pi}{\lambda} \right)^2 (n_{\text{eff}}^2 - n_{\text{air}}^2)$ and J_n, K_n are Bessel functions.

This equation can be reduced, still for the HE_{11} vectorial mode, as

$$f(n_{\text{eff}}, \lambda) = x_r + b_r(1 - \Delta) + \sqrt{b_r^2 \Delta^2 + \frac{c_r}{n_{\text{silica}}^2}} = 0, \quad (\text{B2})$$

$$\begin{aligned} \Delta\beta(\omega_P, \omega_S, \omega_I) &= (\omega_S - \omega_{S0})(\beta_{P0}^{(1)} - \beta_{S0}^{(1)}) - (\omega_I - \omega_{I0})(\beta_{P0}^{(1)} - \beta_{I0}^{(1)}) + 2 \sum_{k=2}^N \frac{(\omega_P - \omega_{P0})^k}{k!} \beta_{P0}^{(k)} \\ &\quad - \sum_{k=2}^N \frac{(\omega_S - \omega_{S0})^k}{k!} \beta_{S0}^{(k)} - \sum_{k=2}^N \frac{(\omega_I - \omega_{I0})^k}{k!} \beta_{I0}^{(k)}, \end{aligned} \quad (\text{B4})$$

which generalizes at all dispersion orders the first-order expression $\Delta\beta_1(\omega_P, \omega_S, \omega_I) = (\omega_S - \omega_{S0})(\beta_{P0}^{(1)} - \beta_{S0}^{(1)}) - (\omega_I - \omega_{I0})(\beta_{P0}^{(1)} - \beta_{I0}^{(1)})$ usually found in the literature [45] [we can note that the high-order terms for the pump can be considered as negligible as usually the pump spectral width can be considered as small enough for the dispersion influence to be limited to the group velocity $v_g(\omega_{p0}) = \frac{1}{\beta_{p0}^{(1)}}$ term].

We can even go further, if we note that the ZDW and thus the emitted wavelength depend on the nanofiber radius. At first order for a small amplitude of the radius fluctuation, the dependence is linear [Fig. 6(b)] and the linear shift of the ra-

dius will also linearly control the dispersion curve and the emitted wavelength shift. If the zero dispersion frequency is shifted by a quantity $\Delta\omega_{\text{ZDW}}$ the new propagation constant $\beta^S(\omega)$ of the dispersion shifted waveguide will be given by

With wavelength independent core and cladding refractive indices the equation is solved as a function of the reduced variables U and V and the effective index is deduced, with a simple relation to the nanofiber radius and a general solution valid whatever this radius.

When dispersion of the different media [$n_{\text{silica}}(\lambda)$ [47] and even $n_{\text{air}}(\lambda)$ [48]] are taken into account, we lose this simple relation and the effective index wavelength dependence has to be calculated for each radius, by solving the implicit Eq. (B2) for the variable $(n_{\text{eff}}, \lambda)$. The equation is solved numerically for some specific points related to the zeros of a Chebyshev polynomial and a development of $n_{\text{eff}}(\lambda)$ [or of the propagation constant $\beta(\omega) = \frac{\omega}{c} n_{\text{eff}}(\frac{2\pi c}{\omega})$] on the basis of Chebyshev polynomials is then realized and used for further calculations (Fig. 6).

In addition, to give a way to numerically simulate the performance of the nanofiber, the polynomial expression of $\beta(\omega)$ allows us to obtain simple analytical expressions for the quantity allowing us to describe more completely the nanofiber behavior when some parameters are varied (such as, for example, in the case of a fluctuation of the radius). $\beta(\omega)$ can be rewritten around a mean frequency ω_{X0} (with $X = P, S, \text{ or } I$):

$$\beta(\omega_X) = \beta_{X0}^{(0)} + (\omega_X - \omega_{X0}) \beta_{X0}^{(1)} + \sum_{k=2}^N \frac{(\omega_X - \omega_{X0})^k}{k!} \beta_{X0}^{(k)}, \quad (\text{B3})$$

where $\beta_{X0}^{(k)} = \frac{\partial^k \beta}{\partial \omega^k}(\omega_{X0})$, and N is the order of the polynomial used to describe $\beta(\omega)$ [we use the fact that $\frac{\partial^{N+1} \beta}{\partial \omega^{N+1}}(\omega) = 0$].

We can then calculate $\Delta\beta(\omega_P, \omega_S, \omega_I) = 2\beta(\omega_P) - \beta(\omega_S) - \beta(\omega_I)$ and obtain, around the wavelength of perfect phase matching (i.e., for $2\beta_{P0}^{(0)} - \beta_{S0}^{(0)} - \beta_{I0}^{(0)} = 0$ and $2\omega_{P0} = \omega_{S0} - \omega_{I0}$),

dius will also linearly control the dispersion curve and the emitted wavelength shift. If the zero dispersion frequency is shifted by a quantity $\Delta\omega_{\text{ZDW}}$ the new propagation constant $\beta^S(\omega)$ of the dispersion shifted waveguide will be given by

$$\beta^S(\omega) = \beta(\omega - \Delta\omega_{\text{ZDW}}) = \beta(\omega) - \Delta\omega_{\text{ZDW}} \frac{\partial \beta}{\partial \omega}(\omega). \quad (\text{B5})$$

We will then be able to write the phase mismatch at first order of $\Delta\omega_{\text{ZDW}}$, as

$$\begin{aligned} \Delta\beta^S(\omega_P, \omega_S, \omega_I, \Delta\omega_{\text{ZDW}}) \\ = \Delta\beta(\omega_P, \omega_S, \omega_I) + \Delta\omega_{\text{ZDW}} d\Delta\beta(\omega_P, \omega_S, \omega_I), \end{aligned} \quad (\text{B6})$$

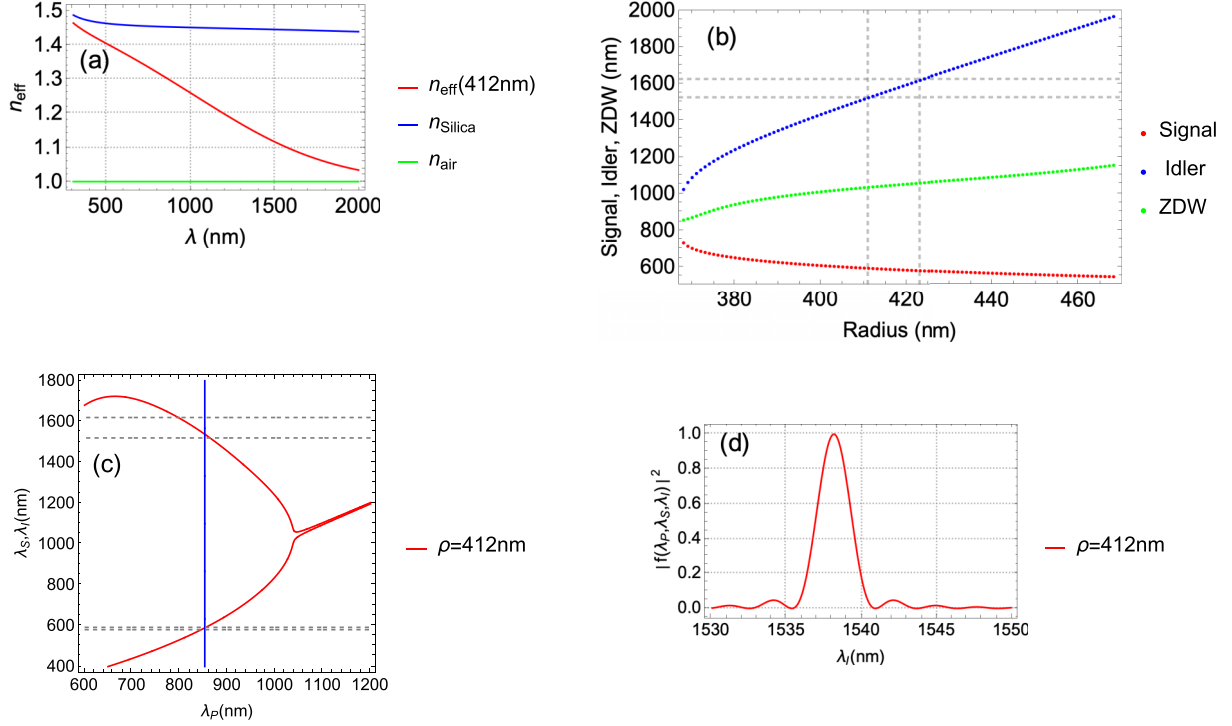


FIG. 6. (a) Simulated value of the fundamental HE11 mode effective index for a nanofiber radius of 412 nm. n_{eff} varies from the silica refractive index at wavelengths where the mode is highly confined in the nanofiber core, to the air refractive index when the mode is deconfined. (b) From the effective index we can calculate the zero dispersion wavelength as a function of the nanofiber radius (green/light gray curve) and by solving the energy ($\omega_{S0} - \omega_{I0} - 2\omega_{P0} = 0$) and momentum [$2\beta(\omega_{P0}) - \beta(\omega_{S0}) - \beta(\omega_{I0}) = 0$] conservation equation simultaneously we can calculate for each radius the emitted signal (red/gray curve) and idler (blue/dark gray curve) wavelength values as a function of radius for a pump wavelength of 852.2 nm. This allows us to determine the radius range allowing emission of idler photons in the telecom band (gray dashed lines). (c) The same calculation can also be performed for a fixed radius (here 412 nm) as a function of pump wavelength, to evaluate tolerance on pump wavelength. (d) Finally, we can calculate the shape of emission spectra by tracing $\text{Sinc}^2\{[2\beta(\omega_{P0}) - \beta(\omega_S) - \beta(\omega_I)]L/2\}$ for a nanofiber of length $L = 1$ cm at energy conservation.

with

$$d\Delta\beta(\omega_P, \omega_S, \omega_I) = 2\frac{\partial\beta}{\partial\omega}(\omega_P) - \frac{\partial\beta}{\partial\omega}(\omega_S) - \frac{\partial\beta}{\partial\omega}(\omega_I). \quad (\text{B7})$$

Using the relation $\frac{\partial\beta}{\partial\omega}(\omega_X) = \beta_{X0}^{(1)} + \sum_{k=2}^N \frac{(\omega_X - \omega_{X0})^{k-1}}{(k-1)!} \beta_{X0}^{(k)}$, we finally obtain

$$\begin{aligned} d\Delta\beta(\omega_P, \omega_S, \omega_I) &= 2\beta_{P0}^{(1)} - \beta_{S0}^{(1)} - \beta_{I0}^{(1)} + (\omega_S - \omega_{S0})(\beta_{P0}^{(2)} - \beta_{S0}^{(2)}) + (\omega_I - \omega_{I0})(\beta_{P0}^{(2)} - \beta_{I0}^{(2)}) \\ &+ 2\sum_{k=3}^N \frac{(\omega_P - \omega_{P0})^{k-1}}{(k-1)!} \beta_{P0}^{(k)} - \sum_{k=3}^N \frac{(\omega_S - \omega_{S0})^{k-1}}{(k-1)!} \beta_{S0}^{(k)} - \sum_{k=3}^N \frac{(\omega_I - \omega_{I0})^{k-1}}{(k-1)!} \beta_{I0}^{(k)}. \end{aligned} \quad (\text{B8})$$

The fluctuation of the zero dispersion frequency governs the emission spectra at first order through the term $d\Delta\beta_1(\omega_P, \omega_S, \omega_I) = 2\beta_{P0}^{(1)} - \beta_{S0}^{(1)} - \beta_{I0}^{(1)} + (\omega_S - \omega_{S0})(\beta_{P0}^{(2)} - \beta_{S0}^{(2)}) + (\omega_I - \omega_{I0})(\beta_{P0}^{(2)} - \beta_{I0}^{(2)})$.

APPENDIX C: CHARACTERIZATION WITH STIMULATED EMISSION TOMOGRAPHY

Characterization with an SET experiment allows us to precisely locate the emission peak [33,34], through access to the JSI (see Appendix A). For the SET measurement, a tunable spectrally thin seed beam (on the idler side in our case) is

injected together with the pump beam, this beam is amplified through stimulated four-wave mixing, and simultaneously each amplified seed photon is accompanied by a twin photon on the signal side. Usually, the spectrum of these signal photons, corresponding in practice to a slice of the JSI [Fig. 5(c)] at the used seed wavelength, is measured with a spectrometer. The seed wavelength is then varied, and a new spectrum is registered, allowing us to finally reconstruct the JSI [inset in Fig. 7(b)]. Considering the typical spectral width of the pulsed pump beam [typically around 0.25 nm, with largest values at 0.5 nm for shortest pulses [Fig. 7(a)] and the limited resolution of the used fibered spectrometer (Ocean Optics USB2000)

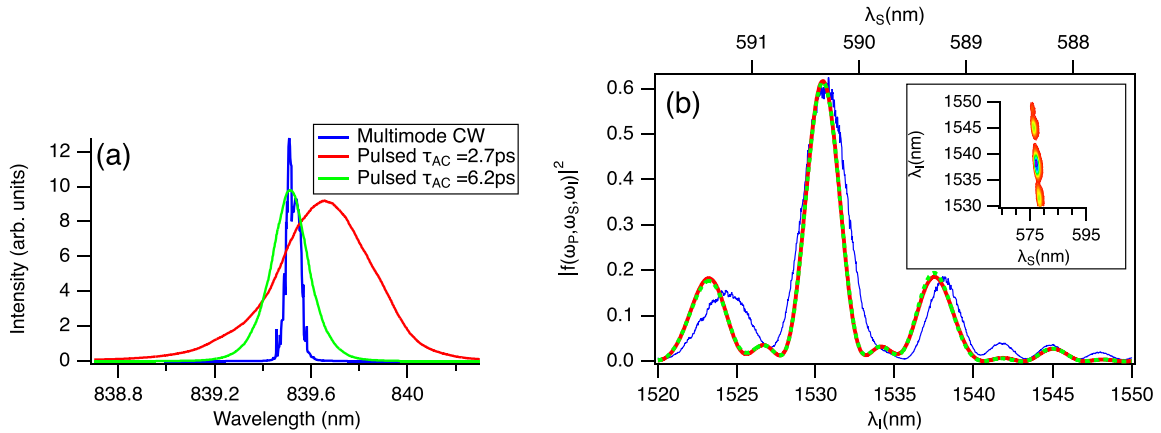


FIG. 7. (a) Typical spectrum of the Ti:sapphire laser in the multimode cw regime, and in the pulsed regime (at two extremal pulse autocorrelation durations). In the cw regime it is only slightly thinner than in the pulsed regime and would give a JSI with a similar width. The single-mode cw laser diode is not shown, as its much thinner spectrum cannot be resolved by our optical spectrum analyzer. (b) Experimental measurement of the photon pairs emission spectra at energy conservation for a pump at 852 nm; λ_I is the tunable laser diode wavelength and λ_S is determined through energy conservation (or by the fibered spectrometer calibration) giving function $|f(\omega_p, 2\omega_p - \omega_I, \omega_I)|^2$ (blue/dark gray curve). Comparison with simulation using a sinusoidal fluctuation of the ZDW along propagation, with period $z_p = 3.83$ mm, amplitude of fluctuation $\Delta\lambda_{ZDW} = 2.2$ nm, and a phase $\phi_0 = -2$ rad; the dashed green/light gray curve represents the calculation with analytical expression (D2), whereas the red/gray curve represents the numerical model of [36]. The inset shows a classical SET spectral map obtained with a fibered spectrometer for a slightly different pump wavelength (around 840 nm) and a slightly more stretched nanofiber. The JSI is characteristic of a correlated state expected for a general phase-matching condition in which group velocity matching is not optimized [34]. The spectral width of the JSI along the signal wavelength axis is limited by the spectral resolution of the used fibered spectrometer and is thus the same for all types of pump.

around 1 nm [inset in Fig. 7(b)], we can hardly resolve the energy conservation contribution to the JSI, and the response is mainly governed by the phase-matching function at energy conservation, which has the well-known sinc shape. That is why we prefer to adapt the classical SET setup, by replacing the spectrometer directly by the single-photon detector of our experiment, used with a 10-nm interferential band-pass filter positioned around the expected response wavelength (it would correspond to integrating the whole spectral response of the spectrometer for each value of the idler wavelength), similar to a projection of the JSI [Fig. 5(c)] on the idler wavelength axis (and converted to the signal wavelength using the energy conservation relation). Due to the very high sensitivity of the single-photon detectors, we can then obtain the JSI at low power and even in the cw regime with high dynamics (the only constraints being that the stimulated response has to overpass the spontaneous one), without losing the spectral resolution given by the much smaller spectral width and by the tuning step of the tunable seed. The tunable laser diode wavelength is tuned at constant speed and fixed wavelength steps and the temporal variation of the single-photon detector count rate is registered. The temporal step being related to the tuning speed, a precise wavelength SET response curve can then be registered. Figure 7(b) shows a typical spectrum we obtained with a pump at 852 nm. We observed no difference in the spectral shape obtained in the pulsed and cw pump regime (with a typical average power in the mW range), indicating negligible influence of Self Phase Modulation pulse broadening in our experimental conditions [49]. The JSI shows a three peak structure [Fig. 7(b)], with the main peak width close to the spectral width expected for our 1-cm nanofiber length [Fig. 6(d)]. We attribute this JSI broadening to nanofiber diameter fluctuations that cause fluctuations of the ZDW of

the nanofiber. Usually, these fluctuations are random, and the peak shape is strongly affected with high chaotic broadening [10,36,50] that most of the time prevents us from reversely determining the fiber fluctuation shape from the JSI shape. In our case, the rather organized shape of the JSI allows us to deduce that our nanofiber presents probably a sinusoidal fluctuation of its diameter (Appendix D).

These preliminary results allow us to optimize the detection setup. Indeed, we can see that the spectral extension of the emitted photons is mostly in a 20-nm band around 1530 nm (and a 3-nm band around 590 nm on the signal side). These bands are well covered by the 1530-nm spectral channel of our commercial CWDM filter (and by a 590-nm band-pass filter of 10-nm bandwidth). This means that almost all the emitted photon pairs can be efficiently detected. We can also note that the main peak width is around 3 nm and that a better filtering of noise is possible at the expense of a moderate loss of coincidences (as only the lateral peaks are lost). Furthermore, we can also accommodate for small fluctuation of the pulsed laser pump wavelength, that we estimate we can control with an accuracy of the order of ± 0.3 nm depending on precise adjustment of the laser cavity on a day-to-day basis, as well as compared to the much more stable cw laser diode frequency (these fluctuations cause an idler wavelength fluctuation of less than ± 0.5 nm that is largely compatible with the spectral width of our filters).

APPENDIX D: DETERMINATION OF THE NANOFIBER SHAPE

To deduce the nanofiber longitudinal shape, we use the expression of the phase-matching function in presence of ZDW

fluctuation, given for a fiber of length L , by [50]

$$f(\omega_P, \omega_S, \omega_I) = \frac{1}{L} \int_0^L dz e^{i \int_0^z \Delta\beta^S(\omega_P, \omega_S, \omega_I, z') dz'}, \quad (\text{D1})$$

where $\Delta\beta^S(\omega_P, \omega_S, \omega_I, z)$ is the position dependent phase mismatch between the different propagating waves. We have to note here that the relation (D1) can be used to calculate the effect on the JSI of a waveguide fluctuation, but that, as the JSI corresponds to an integration of the whole waveguide response, it is not possible to reverse it uniquely and obtain the fluctuation directly from the JSI spectrum. Hypotheses must be made on possible causes of fluctuations knowing the characteristics of the waveguide (for example, in our case, a possible contribution of parts of the tapers instead of the nanofibers or different shapes of fluctuations of the nanofiber); then some signatures of these fluctuations can be searched in the measured JSI, to arbitrate between the different possibilities. For the studied fiber, we finally opt for the simple sinusoidal fluctuation, that gives good accordance with a small number of free parameters, always remembering that more complex fluctuations might probably give a similar JSI at the expense of a larger number of free parameters.

In the general cases, the analysis of this relation is based on numerical models [36] cutting the fiber in small pieces. Nevertheless, in some special cases, such as for a sinusoidal fluctuation, an analytical development can be made.

We write $\Delta\beta^S(\omega_P, \omega_S, \omega_I, z) = \Delta\beta(\omega_P, \omega_S, \omega_I) + \Delta\omega_{ZDW}(z) d\Delta\beta(\omega_P, \omega_S, \omega_I)$, with the position dependent zero dispersion frequency $\Delta\omega_{ZDW}(z) = \Delta\omega_{ZDW0} \sin(\frac{2\pi z}{z_p} + \phi_0)$, and with $\Delta\beta(\omega_P, \omega_S, \omega_I)$ and $d\Delta\beta(\omega_P, \omega_S, \omega_I)$ given by Eqs. (B4) and (B8), respectively (their implicit frequency dependence will be omitted in the following to simplify notations). The fluctuation is then quantified by only three parameters: the amplitude variation of the zero dispersion wavelength $\Delta\lambda_{ZDW0}$ around the mean value λ_{ZDW} of the reference uniform diameter nanofiber, giving $\Delta\omega_{ZDW0} = \frac{2\pi c \Delta\lambda_{ZDW0}}{\lambda_{ZDW}^2}$ (with c the light celerity), the period z_p of the fluctuation, and a phase ϕ_0 related to the exact position of the fluctuation on the nanofiber. We obtain finally after some calculations

$$f(\omega_P, \omega_S, \omega_I) = i e^{i \left(\frac{\Delta\beta L}{2} + \frac{\Delta\omega_{ZDW0} d\Delta\beta z_p \cos(\phi_0)}{2\pi} \right)}$$

$$\begin{aligned} & \times \sum_{n=-\infty}^{n=+\infty} e^{i n \left(\frac{\pi L}{z_p} + \phi_0 + \frac{\pi}{2} \right)} J_n \left(-\frac{\Delta\omega_{ZDW0} d\Delta\beta z_p}{2\pi} \right) \\ & \times \text{Sinc} \left(\frac{\Delta\beta L}{2} + \frac{\pi n L}{z_p} \right). \end{aligned} \quad (\text{D2})$$

In first approximation (i.e., for small fluctuations), the JSI will present side peaks having the usual sinc($\frac{\Delta\beta L}{2}$) shape. The peak amplitude is governed by the Bessel function J_n of order n , with an argument directly related to the product of the amplitude of the fluctuation with the period of the fluctuation. This means that the shorter the fluctuation period, the higher the tolerable amplitude fluctuation. The peak positions are directly related to the fluctuation period z_p (with the condition $\Delta\beta z_p = 2\pi n$, meaning that the peak would be at the zeros of the phase-matching curve of an identical perfect nanofiber of length z_p). Evidently, for high fluctuations, the different terms' contributions mix and the JSI shape will become more chaotic due to the influence of the different phase terms.

If we restrict to the first three orders of the development (0 and ± 1), we find with this model the three observed peaks [Fig. 7(b)]. This response is governed by the dispersion characteristics of the nanofiber. In the simplest model of dispersion [45] using first-order Taylor expansion of the dispersion around the perfect phase-matching frequencies (see Appendix B) we have simply $\Delta\beta = (\omega_S - \omega_{S0})(\beta_{P0}^{(1)} - \beta_{S0}^{(1)}) - (\omega_I - \omega_{I0})(\beta_{P0}^{(1)} - \beta_{I0}^{(1)})$ and $d\Delta\beta = 2\beta_{P0}^{(1)} - \beta_{S0}^{(1)} - \beta_{I0}^{(1)} + (\omega_S - \omega_{S0})(\beta_{P0}^{(2)} - \beta_{S0}^{(2)}) + (\omega_I - \omega_{I0})(\beta_{P0}^{(2)} - \beta_{I0}^{(2)})$, where $\beta_x^{(k)} = \frac{\partial^k \beta}{\partial \omega^k}(\omega_x)$ are known. This allows rapid determination of the fluctuation parameters. Nevertheless, we use in our simulations, as usually done in the literature, higher-order terms in the Taylor development of the dispersion [and larger number of peaks in Eq. (D2)] that gives a little more precise calculation (but without changing fundamentally the behavior) at the expense of more cumbersome expression and less physical insight into the significance of different terms. The spectral structure of the emission spectra can be rather well described by that simple model with a sinusoidal fluctuation of the ZDW with a period of 3.83 mm (around the reference value of $\lambda_{ZDW} = 1036$ nm) and an amplitude of 2.2 nm. Such a variation of the ZDW corresponds to a variation of the diameter of the nanofiber of about ± 2 nm [Fig. 6(b)], around the mean diameter of

TABLE II. Adjustment parameters of the quadratic polynomial fit of experimental data of Fig. 2. The parameters in italic correspond to parameters determined as close to or smaller than their errors bars. The parameters in bold are the ones used to calculate experimental data in Table I.

Source characteristics	Count type	Adjustment linear coefficient b_X (mW ⁻¹ s ⁻¹)	Adjustment quadratic coefficient c_X (mW ⁻² s ⁻¹)
cw single-mode	Signal	<i>0.21 ± 0.25</i>	0.532 ± 0.034
	Idler	1031 ± 14	0.83 ± 2.2
	Coincidence	<i>0 ± 0.017</i>	0.0291 ± 0.0028
cw multimode	Signal	<i>1.72 ± 0.44</i>	1.06 ± 0.06
	Idler	1088 ± 14	0 ± 2.35
	Coincidence	<i>0.0012 ± 0.027</i>	0.0570 ± 0.0044
Sech pulsed	Signal	<i>0 ± 58</i>	2850 ± 43
	Idler	1183 ± 41	1070 ± 20
	Coincidence	<i>0 ± 13</i>	146.5 ± 3.4

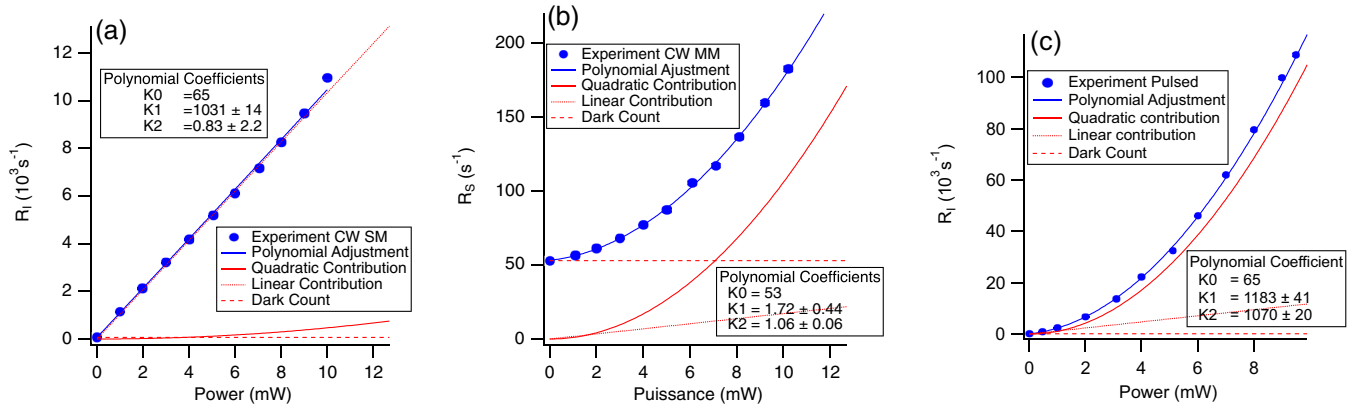


FIG. 8. Polynomial adjustment of the idler (a) experimental count rate of the single-mode cw regime and signal (b) experimental count rate of the multimode cw regime, showing the amplitude of the contribution of the different constant (i.e., dark counts), linear, and quadratic terms. In contrast to Fig. 2, the dark count rate had not been subtracted and the curves are presented in linear scales. For the idler (a), the adjustment shows a small quadratic contribution much smaller than its error bar. The term is considered as not relevant as it is completely masked by the linear contribution. For the signal (b), the roles are exchanged, the linear contribution that is found by adjustment has a large error bar and is considered as irrelevant, as it is completely masked either by the quadratic term (at high power) or by the dark count term (at low power). The main contribution is the quadratic term that is precisely determined, even though its value seems comparable to the equivalent term of the idler. In the case of the idler count rate in the pulsed regime (c), we are in a mixed situation; the linear term can be considered as relevant as it is of the order of the quadratic term at low power but stays higher than the dark count term, but the small number of experimental data in that region where this term dominates probably increase the error bar of the determined coefficient.

824 nm. The origin of this fluctuation is currently unknown; probably it is due to variations of pulling parameters; it may also be due to residual strains in the nanofiber that may cause a change of the ZDW. Moreover, if the sinusoidal fluctuation gives a good idea of the emission spectra the accordance is not perfect and the exact form is probably different, considering that, other periodic fluctuations (square, triangular, etc.) can give spectra with similar shapes. Nevertheless, these results show that our nanofiber is relatively uniform and show an emission spectrum rather close to the ideal sinc shape.

APPENDIX E: COUNTS AND COINCIDENCE DATA ADJUSTMENT PARAMETERS

The experimental points presented in Fig. 2, were adjusted using a third-order polynomial law $R_X = a_X + b_X \bar{I} + c_X \bar{I}^2$, ($X = S, I, C$, for signal, idler, and coincidence) as a function of the pump beam mean power \bar{I} . The adjustment uses the orthogonal distance regression method of fit proposed by our

data treatment software IGORPRO. The adjustment takes into account the error bars on the experimental data and imposes the adjustment coefficients to have a physical significance and thus to be positive.

For the detector count rates, the constant parameter a_X corresponds to the dark count rate that is measured independently and subtracted from the experimental points, so we have a_S and a_I that can be considered to be zero. For the coincidence rate, the expected constant parameter a_C related to dark count accidental coincidences is very small and in practice not measurable in the condition of the presented experiment. It was kept in the adjustment and systematically found to be zero (remembering that we impose this parameter to be positive).

Thus, the only relevant parameters of the adjustment are thus the linear b_X and quadratic c_X parameters; the values of these parameters extracted from the data of Fig. 2 are presented in Table II.

Some of the parameters in the table are much smaller than their error bars; these parameters can thus be considered as

TABLE III. Adjustment parameters of the quadratic polynomial fit of the signal, idler counts, and coincidences rates related to the experimental data of Fig. 4. Note that, contrary to data of Table II, the experimental condition had slightly changed between the two experiments, making the direct comparison of cw and pulsed regimes more difficult. Taking into account the detection efficiencies, the generation rates are, in the pulsed regime $\mu_P = 9.5 \times 10^3$ pairs $s^{-1} mW^{-2}$, and in the cw regime $\mu_P = 6$ pairs $s^{-1} mW^{-2}$, slightly lower than with the pump at 852 nm probably due to a less well-optimized experimental setup.

Source characteristics	Count type	Adjustment linear coefficient b_X ($mW^{-1}s^{-1}$)	Adjustment quadratic coefficient c_X ($mW^{-2}s^{-1}$)
cw multimode	Signal	0 ± 0.07	0.486 ± 0.007
	Idler	9.69 ± 0.11	0 ± 0.0046
	Coincidence	0 ± 0.012	0.0047 ± 0.0001
Sech pulsed	Signal	0 ± 3.1	877 ± 8
	Idler	389 ± 5	378 ± 5
	Coincidence	0.68 ± 0.51	43.32 ± 0.49

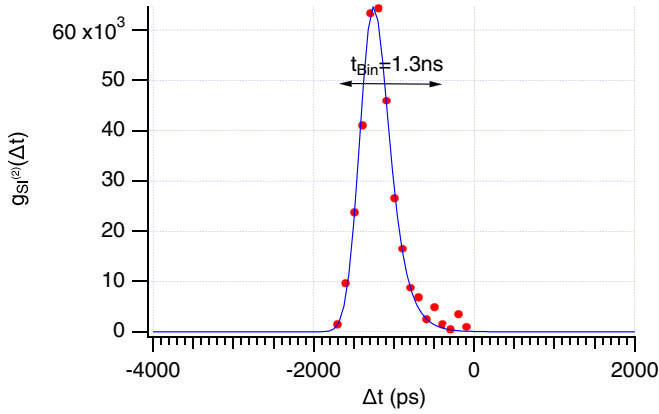


FIG. 9. Plot of the histogram of $g_{SI}^{(2)}$ around the coincidence peak, calculated with a value of $t_{bin} = 100$ ps corresponding to the temporal resolution of our counting and correlation system. The pump power for this measurement was 24 mW, and acquisition time was 240 s. The coincidence peak is fitted by an exponential-convoluted Gaussian function (a preprogrammed function of the multiplex fitting procedure of IGORPRO). It reaches a peak value around 65 000 but is clearly larger than the temporal resolution value. The CAR value obtained with a value of $t_{bin} = 1300$ ps would lead to a reduced value of 24 000 that seems to us more representative of the real performances of our source.

not relevant. This may correspond to a contribution that can reasonably be considered as nonexistent, such as, for example, the linear coefficient of the coincidences rates. This can also be a parameter that corresponds to a minor contribution compared to the other one in the conditions of the experiment. This is illustrated in Figs. 8(a) and 8(b), where we see that the quadratic component of the idler is almost not visible or for the signal where the linear component is much smaller than both quadratic and dark count ones. In both cases, the numerical adjustment can find a value for the corresponding parameters, but we cannot be confident in the found value. Some cases are less clear, for example, the idler count rate in the pulsed regime in Fig. 8(c), where the linear contribution is only visible at low power and would have probably required more experimental points in that range to decrease the error bar.

The signal, idler counts, and coincidence rate parameters associated to the CAR data of Fig. 4 are shown in Table III; we have similar but slightly lower performance compared to experiment at 852 nm, probably because of a less optimized experiment and a longer pulse duration. We can note that the Raman contribution (measured by the idler count rate) is almost two orders of magnitude smaller, thanks to a larger wavelength shift and a better noise filtering.

APPENDIX F: ALTERNATE ANALYSIS OF THE $g_{SI}^{(2)}$ AND COMPARISON TO PRESENT STATE OF THE ART

We found very high CAR values measured in the cw and pulsed regime in a fibered structure geometry, using a rather conservative analysis procedure especially for the cw regime. Indeed, we use a value of t_{bin} that allows us to cover the whole coincidence peak, but also gives a higher value for the noise counts (in the pulsed regime, the accidentals are, except perhaps at the lowest power, governed by peaks with similar shape compared to the coincidence peak so the value taken for t_{bin} is less critical).

To illustrate this point and compare our results to data that presently represent the state of the art in similar structures, we use for the cw regime a data treatment similar to the one used in Ref. [10], i.e., we plot $g_{SI}^{(2)}(\Delta t) = \frac{R_C(\Delta t)}{R_S R_I t_{bin}}$ with a t_{bin} value given by the temporal resolution of the coincidence measurement device (100 ps in our case) (Fig. 9). This treatment would have given a peak value of 65 000, i.e., around 2.7 times better than the maximum value of the CAR (or $g_{SI}^{(2)}$) of 24 000 we measured for the same set of experimental data. This better signal to noise ratio is obtained at the expense of a smaller number of detected pairs since the coincidence peak as a larger width and some coincidences are then outside t_{bin} . That value favorably compares to the performances found in the literature [10] even without considering the factor of 2 enhancement brought by the multimode nature of the used pump source, that partially compensates for the lower quantum efficiency of the InGaAs detector we used, compared to superconducting nanowire single-photon detectors.

This analysis also shows that in the field of experimental characterization of CAR and $g_{SI}^{(2)}$ the measurement procedures are still not completely normalized and that comparison of presented data from different sources with different structures must be realized carefully.

-
- [1] A. S. Helmy, P. Abolghasem, J. Stewart Aitchison, B. J. Bijlani, J. Han, B. M. Holmes, D. C. Hutchings, U. Younis, and S. J. Wagner, Recent advances in phase matching of second-order nonlinearities in monolithic semiconductor waveguides, *Laser Photonics Rev.* **5**, 272 (2011).
- [2] E. Pomarico, B. Sanguinetti, T. Guerreiro, R. Thew, and H. Zbinden, MHz rate and efficient synchronous heralding of single photons at telecom wavelengths, *Opt. Express* **20**, 23846 (2012).
- [3] A. Orioux, M. A. Versteegh, K. D. Jöns, and S. Ducci, Semiconductor devices for entangled photon pair generation: A review, *Rep. Prog. Phys.* **80**, 076001 (2017).
- [4] A. Anwar, C. Perumangatt, F. Steinlechner, T. Jennewein, and A. Ling, Entangled photon-pair sources based on three-wave mixing in bulk crystals, *Rev. Sci. Instrum.* **92**, 041101 (2021).
- [5] H. Takesue, Entangled photon pair generation using silicon wire waveguides, *IEEE J. Sel. Top. Quantum Electron.* **18**, 1722 (2012).
- [6] C. Ma, X. Wang, V. Anant, A. D. Beyer, M. D. Shaw, and S. Mookherjea, Silicon photonic entangled photon-pair and heralded single photon generation with $CAR > 12,000$ and $g(2)(0) < 0.006$, *Opt. Express* **25**, 32995 (2017).
- [7] J. G. Rarity, J. Fulconis, J. Dulligall, W. J. Wadsworth, and P. S. J. Russell, Photonic crystal fiber source of correlated photon pairs, *Opt. Express* **13**, 534 (2005).

- [8] S. D. Dyer, B. Baek, and S. W. Nam, High-brightness, low-noise, all-fiber photon pair source, *Opt. Express* **17**, 10290 (2009).
- [9] S. Dong, Q. Zhou, W. Zhang, Y. He, W. Zhang, L. You, Y. Huang, and J. Peng, Energy-time entanglement generation in optical fibers under CW pumping, *Opt. Express* **22**, 359 (2014).
- [10] J. Hammer, M. V. Chekhova, D. R. Häupl, R. Pennetta, and N. Y. Joly, Broadly tunable photon-pair generation in a suspended-core fiber, *Phys. Rev. Research* **2**, 012079 (2020).
- [11] S. Dong, L. Yu, W. Zhang, J. Wu, W. Zhang, L. You, and Y. Huang, Generation of hyper-entanglement in polarization/energy-time and discrete-frequency/energy-time in optical fibers, *Sci. Rep.* **5**, 9195 (2015).
- [12] J. E. Sharping, K. F. Lee, M. A. Forster, A. C. Turner, B. S. Schmidt, M. Lipson, A. L. Gaeta, and P. Kumar, Generation of correlated photons in nanoscale silicon waveguides, *Opt. Express* **14**, 12388 (2006).
- [13] M. Barbier, I. Zaquine, and P. Delaye, Spontaneous four-wave mixing in liquid-core fibers: Towards fibered Raman-free correlated photon sources, *New J. Phys.* **17**, 053031 (2015).
- [14] M. A. Finger, T. S. Iskhakov, N. Y. Joly, M. V. Chekhova, and P. S. J. Russell, Raman-Free, Noble-Gas-Filled Photonic-Crystal Fiber Source for Ultrafast, Very Bright Twin-Beam Squeezed Vacuum, *Phys. Rev. Lett.* **115**, 143602 (2015).
- [15] M. Cordier, P. Delaye, F. Gérôme, F. Benabid, and I. Zaquine, Raman-free fibered photon-pair source, *Sci. Rep.* **10**, 1650 (2020).
- [16] C. Söller, B. Brecht, J. Mosley, L. Y. Zang, A. Podlipensky, N. Y. Joly, S. J. Russell, and C. Silberhorn, Bridging visible and telecom wavelengths with a single-mode broadband photon pair source, *Phys. Rev. A* **81**, 031801 (2010).
- [17] J. Lugani, R. J. Francis-Jones, J. Boutari, and I. A. Walmsley, Spectrally pure single photons at telecommunications wavelengths using commercial birefringent optical fiber, *Opt. Express* **28**, 5147 (2020).
- [18] L. Tong, F. Zi, X. Guo, and J. Lou, Optical microfibers and nanofibers: A tutorial, *Optics Communications* **285**, 4641 (2012).
- [19] F. Xu, Z. X. Wu, and Y. Q. Lu, Nonlinear optics in optical-fiber nanowires and their applications, *Prog. Quantum Electron.* **55**, 35 (2017).
- [20] K. P. Nayak, M. Sadgrove, R. Yalla, F. Le Kien, and K. Hakuta, Nanofiber quantum photonics, *J. Opt.* **20**, 073001 (2018).
- [21] A. Azzoune, P. Delaye, and G. Pauliat, Optical microscopy for measuring tapered fibers beyond the diffraction limit, *Opt. Express* **27**, 24403 (2019).
- [22] D. Lee, K. J. Lee, J. H. Kim, K. Park, D. Lee, Y. H. Kim, and H. Shin, Fabrication method for ultra-long optical micro/nanofibers, *Curr. Appl Phys.* **19**, 1334 (2019).
- [23] L. Cui, X. Li, C. Guo, Y. H. Li, Z. Y. Xu, L. J. Wang, and W. Fang, Generation of correlated photon pairs in micro/nanofibers, *Opt. Lett.* **38**, 5063 (2013).
- [24] J. H. Kim, Y. S. Ihn, Y. H. Kim, and H. Shin, Photon-pair source working in a silicon-based detector wavelength range using tapered micro/nanofibers, *Opt. Lett.* **44**, 447 (2019).
- [25] E. Ortiz-Ricardo, C. Bertoni-Ocampo, Z. Ibarra-Borja, R. Ramirez-Alarcon, D. Cruz-Delgado, H. Cruz-Ramirez, K. Garay-Palmett, and A. B. U'ren, Spectral tunability of two-photon states generated by spontaneous four-wave mixing: Fibre tapering, temperature variation and longitudinal stress, *Quantum Science and Technology* **2**, 034015 (2017).
- [26] J. Su, L. Cui, Y. Li, and X. Li, Micro/nano-fiber-based source of heralded single photons at the telecom band, *Chinese Optics Letters* **16**, 041903 (2018).
- [27] A. A. Shukhin, J. Keloth, K. Hakuta, and A. A. Kalachev, Heralded single-photon and correlated-photon-pair generation via spontaneous four-wave mixing in tapered optical fibers, *Phys. Rev. A* **101**, 053822 (2020).
- [28] W. P. Grice and I. A. Walmsley, Spectral information and distinguishability in type-II down-conversion with a broadband pump, *Phys. Rev. A* **56**, 1627 (1997).
- [29] M. Bouhadida, P. E. Verdier, and S. Lebrun, Laser-induced damage in silica nanofibers in air and immersed in different liquids in the nanosecond regime, *IEEE Photon. Technol. Lett.* **33**, 967 (2021).
- [30] M. Bouhadida, J. C. Beugnot, P. Delaye, K. Phan Huy, and S. Lebrun, Highly efficient and reproducible evanescent Raman converters based on a silica nanofiber immersed in a liquid, *Appl. Phys. B* **125**, 228 (2019).
- [31] M. Bouhadida, P. Delaye, and S. Lebrun, Long-term optical transmittance measurements of silica nanofibers, *Optics Communications* **500**, 127336 (2021).
- [32] M. Liscidini and J. E. Sipe, Stimulated Emission Tomography, *Phys. Rev. Lett.* **111**, 193602 (2013).
- [33] B. Fang, O. Cohen, M. Liscidini, J. E. Sipe, and V. O. Lorenz, Fast and highly resolved capture of the joint spectral density of photon pairs, *Optica* **1**, 281 (2014).
- [34] M. Cordier, A. Orieux, B. Debord, F. Gérôme, A. Gorse, M. Chafer, E. Diamanti, P. Delaye, F. Benabid, and I. Zaquine, Active engineering of four-wave mixing spectral correlations in multiband hollow-core fibers, *Opt. Express* **27**, 9803 (2019).
- [35] T. Lunghi, C. Barreiro, O. Guinnard, R. Houlmann, X. Jiang, M. A. Itzler, and H. Zbinden, Free-running single-photon detection based on a negative feedback InGaAs APD, *J. Mod. Opt.* **59**, 1481 (2012).
- [36] L. Cui, X. Li, and N. Zhao, Spectral properties of photon pairs generated by spontaneous four-wave mixing in inhomogeneous photonic crystal fibers, *Phys. Rev. A* **85**, 023825 (2012).
- [37] SPDC810 manual, <https://www.thorlabs.com/drawings/c128100598062727-72FC153D-C75E-86E1-1A4E306DB2A2AB7D/SPDC810-Manual.pdf>.
- [38] Y. Q. Xu and S. G. Murdoch, Gain spectrum of an optical parametric amplifier with a temporally incoherent pump, *Opt. Lett.* **35**, 169 (2010).
- [39] K. Hammani, A. Picozzi and C. Finot, Extreme statistics in Raman fiber amplifiers: From analytical description to experiments, *Optics Communications* **284**, 2594 (2011).
- [40] A. A. Grütter, H. P. Weber and R. Dändliker, Imperfectly mode-locked laser emission and its effects on nonlinear optics, *Phys. Rev.* **185**, 629 (1969).
- [41] L. Mandel and E. Wolf, Coherence properties of optical fields, *Rev. Mod. Phys.* **37**, 231 (1965).
- [42] M. C. Phan Huy, A. Baron, S. Lebrun, R. Frey, and P. Delaye, Characterization of self-phase modulation in liquid filled hollow core photonic bandgap fibers, *JOSA B* **27**, 1886 (2010).
- [43] L. G. Helt, M. Liscidini, and J. E. Sipe, How does it scale? Comparing quantum and classical nonlinear optical processes in integrated devices, *J. Opt. Soc. Am. B* **29**, 2199 (2012).

- [44] M. Corona, K. Garay-Palmett, and A. B. U'Ren, Third-order spontaneous parametric down-conversion in thin optical fibers as a photon-triplet source, *Phys. Rev. A* **84**, 033823 (2011).
- [45] K. Garay-Palmett, H. J. McGuinness, O. Cohen, J. S. Lundeen, R. Rangel-Rojo, A. B. U'ren, M. G. Raymer, C. J. McKinstrie, S. Radic, and I. A. Walmsley, Photon pair-state preparation with tailored spectral properties by spontaneous four-wave mixing in photonic-crystal fiber, *Opt. Express* **15**, 14870 (2007).
- [46] A. W. Snyder and J. Love, *Optical Waveguide Theory* (Springer, New York, 2012).
- [47] I. H. Malitson, Interspecimen comparison of the refractive index of fused silica, *JOSA* **55**, 1205 (1965).
- [48] P. E. Ciddor, Refractive index of air: New equations for the visible and near infrared, *Appl. Opt.* **35**, 1566 (1996).
- [49] B. Bell, A. McMillan, W. McCutcheon, and J. Rarity, Effects of self-and cross-phase modulation on photon purity for four-wave-mixing photon pair sources, *Phys. Rev. A* **92**, 053849 (2015).
- [50] M. S. M. Santandrea, V. Ansari, and C. Silberhorn, Fabrication limits of waveguides in nonlinear crystals and their impact on quantum optics applications, *New J. Phys.* **21**, 033038 (2019).